



One-step hydrothermal synthesis of high-percentage 1T-phase MoS₂ quantum dots for remarkably enhanced visible-light-driven photocatalytic H₂ evolution

Xitao Li^{a,b}, Xinding Lv^{a,b}, Nan Li^{a,b}, Jiaojiao Wu^{a,b}, Yan-Zhen Zheng^{a,c,*}, Xia Tao^{a,b,c,*}

^a Beijing Advanced Innovation Center for Soft Matter Science and Engineering, Beijing University of Chemical Technology, Beijing 100029, China

^b State Key Laboratory of Organic-Inorganic Composites, Beijing University of Chemical Technology, Beijing 100029, China

^c Research Center of the Ministry of Education for High Gravity Engineering & Technology, Beijing University of Chemical Technology, Beijing 100029, China

ARTICLE INFO

Keywords:

MoS₂ quantum dot
High-percentage metallic phase
Visible light
H₂ evolution

ABSTRACT

Molybdenum disulfide (MoS₂) are proven to be a promising non-precious-metal cocatalyst for the photocatalytic hydrogen evolution reaction (HER), but the catalytic efficiency of reported MoS₂ is still poor due to its limited active sites and low conductivity. Herein, we report a facile one-step hydrothermal approach for synthesizing water-dispersed high-percentage metallic 1T-phase MoS₂ quantum dots at a reaction temperature of 180 °C (denoted as 1T-MoS₂ QDs-180). Such prepared 1T-MoS₂ QDs-180 possesses well-dispersed ultrasmall size of ~3.3 nm and 1T-phase composition over 82%. Benefiting from the abundance of exposed catalytic edge sites, as well as the excellent intrinsic conductivity of 1T-MoS₂ QDs-180, the preformed heterostructure photocatalyst i.e. 1T-MoS₂ QDs-180 loading onto CdS nanorods (denoted as 1T-MoS₂-C) exhibits remarkably enhanced visible-light ($\lambda > 420$ nm) photocatalytic HER in comparison with pure CdS. Particularly, the HER rate of the optimized 3 wt.% 1T-MoS₂-C reaches climbing up to 131.7 mmol h⁻¹ g⁻¹, over 65-fold the rate of pure CdS (2.0 mmol h⁻¹ g⁻¹) and appropriately 2-fold the rate of precious-metal Pt loaded CdS (67.0 mmol h⁻¹ g⁻¹). To the best of our knowledge, our home-made 1T-MoS₂-C photocatalyst shows the highest visible-light-driven HER performance among all reported phase-engineered MoS₂ photocatalytic systems. Such a simple and propagable hydrothermal approach capable of achieving the ultrasmall-sized metallic phase transition metal dichalcogenides is applicable in green hydrogen energy production.

1. Introduction

Since the pioneering work of photoelectrochemical water splitting on TiO₂ electrode reported by Fujishima and Honda in 1972 [1], the conversion of solar energy into perfect hydrogen (H₂) energy via photocatalytic water splitting using semiconductors as catalysts has attracted great attention [2–5]. Generally, a photocatalytic reaction on a semiconductor includes at least three main steps: 1) absorption of light by semiconductor to produce electron-hole pairs, 2) charge separation and migration to the surface of semiconductor, and 3) surface reactions for water reduction or oxidation [6]. However, bare photocatalysts (e.g. CdS, TiO₂, g-C₃N₄) shows extremely low activity for photocatalytic hydrogen evolution reaction (HER) due to its rapid photogenerated electron-hole recombination and lack of active sites for proton reduction [7–9]. Integration of noble metal-based cocatalysts (e.g. Pt, Au, Pd) on semiconductor material has proven to be an effective way for

suppressing electron-hole recombination and accelerating photocatalytic HER [10]. However, scale-up application of the commonly-used noble metal cocatalysts is still tough because of their scarceness and high-cost.

As a typical layered transition metal disulfide, MoS₂, has been demonstrated to be a promising cocatalyst alternative to noble metal due to its free energy similar to Pt, earth-abundant composition and explicit catalytic mechanism [11–18]. The commonly-used MoS₂ for photocatalytic HER is 2H-phase, exhibiting semiconductor properties with a tunable bandgap ranging from 1.3 eV to 1.9 eV. Both theoretical [19] and experimental [20] studies have demonstrated that catalytically active sites of 2H-MoS₂ are located along the edges of the MoS₂ layers while basal surfaces are ineffective for catalytic reactions. To date, great efforts have been made to boost the exposed active edge sites of the MoS₂, for example, either through fabricating small-sized nanoparticles [21], nanosheets [22], nanoflowers [23], and defect-rich

* Corresponding author at: Beijing Advanced Innovation Center for Soft Matter Science and Engineering, Beijing University of Chemical Technology, Beijing 100029, China.

E-mail addresses: taoxia@mail.buct.edu.cn, taoxia@yahoo.com (X. Tao).

<https://doi.org/10.1016/j.apcatb.2018.10.033>

Received 25 July 2018; Received in revised form 2 October 2018; Accepted 14 October 2018

Available online 15 October 2018

0926-3373/ © 2018 Elsevier B.V. All rights reserved.

nanosheets [24], or through introducing sulfur vacancies and doping/alloying into the inert basal plane of 2H-phase MoS₂ [25,26]. Besides, inherent semi-conductive character of 2H-MoS₂ i.e. poor conductivity also restricts the fast electron/charge injection/transfer during the catalytic HER process. In view of this, the strategies to improve the MoS₂ conductivity have been also performed by applying conductive supports such as Au [27], carbon paper [28–30], or graphene [31,32]. Despite these aforementioned efforts, the HER performance of 2H MoS₂-based photocatalysts is still dissatisfactory, which requires more exploration urgently [33,34].

MoS₂ quantum dots (denoted as MoS₂ QDs) has attracted more significant attention due to its larger specific surface area, better solubility in aqueous solvents, and more edge atoms compared with other MoS₂ nanostructures or bulk-MoS₂. The reported strategies for preparing MoS₂ QDs included hydrothermal synthesis [35], lithium intercalation [36], and liquid exfoliation in organic solvents [37]. For example, MoS₂ QDs was prepared by Ren et al. via hydrothermal method, exhibiting good electrocatalytic activity for the HER [38]. Sun et al. adopted liquid exfoliation strategy to obtain MoS₂ QDs, and achieved a photocatalytic hydrogen production activity with a rate of 0.206 mmol h⁻¹ g⁻¹ over CdS [39]. It should be pointing out that almost all pioneering work on MoS₂ QDs focused on 2H-phase, and the catalytic efficiency of semiconducting 2H-phase MoS₂ QDs cocatalysts was still restricted by its low intrinsic electrical conductivity. A straightforward way to settle this fundamental issue is to prepare metallic 1T-phase MoS₂ quantum dots (denoted as 1T-MoS₂ QDs) via phase engineering since the high electrical conductivity of metallic 1T-MoS₂ QDs can facilitate the fast electron/charge injection/transfer during the photocatalytic HER process. To date, only one work concerning 1T-MoS₂ QDs was performed by Zhang's group [40], in which they demonstrated the excellent electrochemical HER performances for 1T-MoS₂ QDs with 1T-phase composition of ~70%. Although an impressive electrochemical catalytic performance has been achieved, the tedious complicated Li-intercalation and time-consuming preparation procedure for high-percentage 1T-MoS₂ QDs was involved. Thus, it remains a challenge to develop a fast, facile and one-step solution process to synthesize high-percentage 1T-MoS₂ QDs with abundant active edge sites and good electronic conductivity for photocatalytic hydrogen production application.

In our previous exploration of defect-rich/defect-free 1T-MoS₂ nanosheets [41], we found that temperature was a key parameter influencing on the MoS₂ phase transition between 1T and 2H during the hydrothermal synthesis. Inspired by this, we herein experimentally tune the hydrothermal reaction temperature and successfully obtain water-dispersed high-percentage metallic 1T-MoS₂ QDs at a temperature of 180 °C (i.e. 1T-MoS₂ QDs-180). The preparation procedure is schematically illustrated in Fig. 1. A series of characterization results (i.e. TEM, Raman, XPS) show that the obtained 1T-MoS₂ QDs-180 possesses well-

dispersed ultrasmall size of ~3.3 nm and a high-percentage 1T-phase composition over 82%. Impressively, the preformed heterostructure photocatalyst i.e. 1T-MoS₂-C exhibits remarkably enhanced visible-light ($\lambda > 420$ nm) photocatalytic HER efficiency in comparison with pure CdS as well as good stability in the photocatalytic cyclic runs. Particularly, the HER rate of the optimized 3 wt.% 1T-MoS₂-C reaches climbing up to 131.7 mmol h⁻¹ g⁻¹, over 65-fold the rate of pure CdS (2.0 mmol h⁻¹ g⁻¹) and appropriately 2-fold the rate of precious-metal Pt loaded CdS (67.0 mmol h⁻¹ g⁻¹). In addition, a possible mechanism for efficient photocatalytic H₂ evolution process over 1T-MoS₂-C composites is proposed. In short, the 1T-MoS₂ QDs-180 not only act as electron delivery channels with high electrical conductivity, but also offer abundant reaction sites for H₂ production, consequently contributing to the excellent HER performance of 1T-MoS₂-C.

2. Experimental section

2.1. Materials synthesis

2.1.1. Preparation of MoS₂ QDs-170, 1T-MoS₂ QDs-180, MoS₂ QDs-200, MoS₂ QDs-220

1T-MoS₂ QDs was fabricated by controlling the hydrothermal reaction temperature. Specifically, 0.4 g of Na₂MoO₄·2H₂O was dissolved in 30 mL deionized water with ultrasonication for 30 min. Then, 0.38 g of C₁₄H₁₄S₂ dissolved in 30 mL ethanol was added to the above solution. After sonicating for 30 min, the mixture was then transferred to a 100 mL Teflon-lined stainless steel autoclave and heated at 180 °C for 20 h. After that, 30 mL deionized water was added to disperse black product. The resulting suspension was then centrifuged for 90 min at 10,000 rpm to separate the supernatant and centrifugate. The obtained supernatant was denoted as 1T-MoS₂ QDs-180 solution. To determine the concentration of 1T-MoS₂ QDs-180 solution, the solution was treated by freeze drying to gain powder (6.0 mg with the yield of 2.28%). As thus, in terms of the powder weight and the volume of supernatant before freeze drying, the concentration of as-prepared 1T-MoS₂ QDs-180 solution is determined to be ca. 0.2 mg mL⁻¹. In parallel, the samples obtained at 170 °C, 200 °C and 220 °C are marked with MoS₂ QDs-170, MoS₂ QDs-200 and MoS₂ QDs-220, respectively. Note that MoS₂ QDs-170 was not chosen for further investigation because only a few MoS₂ QDs-170 (i.e. 0.9 mg) was obtained.

2.1.2. Preparation of CdS

CdS was fabricated by a hydrothermal method [42]. Briefly, 20 mmol CdCl₂·2.5H₂O and 60 mmol NH₂CSNH₂ were added into a 100 mL Teflon-lined stainless-steel autoclave containing 60 mL ethylenediamine. Then, the autoclave was heated at 160 °C for 48 h, resulting in yellow precipitate. After rinsing by ethanol and deionized water and drying at 60 °C for 12 h, CdS powder was finally obtained.

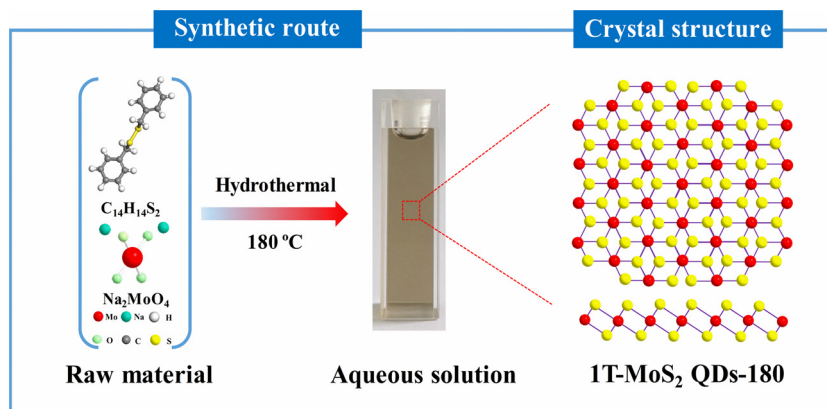


Fig. 1. Schematic illustration of synthetic route for high-percentage 1T-MoS₂ QDs-180 through a hydrothermal technique.

2.1.3. Preparation of 1T-MoS₂-C photocatalyst

Composite photocatalysts were prepared via ultrasonic mixing, as schematically shown in Fig. S1. Generally, 100 mg CdS and 15.0 mL (0.2 mg mL⁻¹) of as-prepared 1T-MoS₂ QDs-180 solution were mixed and then sonicated for 2 h. Subsequently, the obtained mixture was centrifuged and dried at 60 °C to gain the target product (3 wt.% 1T-MoS₂-C). Similarly, a series of hybrid catalysts, including 0.5 wt.%, 1 wt.%, 5 wt.% and 7 wt.% 1T-MoS₂-C, were obtained by adjusting the volume of 1T-MoS₂ QDs-180 solution as 2.5, 5.0, 25.0 and 35.0 mL, respectively.

2.2. Characterizations

The obtained samples were characterized by X-ray diffraction (XRD) (X'Pert PRO MPD, Panalytical) utilizing Cu K α radiation at a scan rate of 5° min⁻¹. The absorption spectra of the photocatalysts were acquired from UV-vis spectrophotometer (Perkin Elmer Lambda 950 UV-vis). The morphology and crystal structure of samples were characterized by transmission electron microscopy (TEM) and high resolution TEM (HRTEM) (JEOL JEM-3010), and its composition was examined using energy-dispersive spectroscopy (EDS) attached to the TEM instrument. The phase information was obtained from X-ray photoelectron spectroscopy (XPS) (Thermo ESCALAB250) and Raman spectra that were performed using a LabRAMHR-800 of French company HRIBA with a 514 nm laser. All photoluminescence (PL) spectra measurement were performed on a Hitachi F7000 fluorescence spectrofluorometer. Zeta-potential of the as-prepared samples in deionized water were measured on a Malvern zeta analyzer (Nano-ZS 90, Malvern Instrument, UK). AFM measurements were conducted on a Bruker Multimode 8 with ScanAsyst scanning probe microscope. The Brunauer, Emmett and Teller (BET) surface area of the samples were taken using a Quantachrome Quadrasorb SI instrument and calculated by multi-point estimation.

2.3. Photoelectrochemical measurements

Photoelectrochemical performance was measured using an electrochemical analyzer (CHI660C) in a homemade standard three-electrode quartz cell with a H₂SO₄ (cocatalyst system) or Na₂SO₄ (composite catalyst system) electrolyte solution and a saturated calomel electrode (SCE) as the reference electrode. As for photoelectrochemical measurement for MoS₂ QDs, a graphite rod were the counter electrode. For preparation of the working electrode, 1 mL MoS₂ QDs were firstly mixed 25 μ L Nafion solution (5 wt.%) under sonication for 20 min, and then 20 μ L of the resulting solution was drop cast onto the glassy carbon electrode (GCE) and dried at room temperature to form the MoS₂ QDs electrode. For comparison, the bulk-MoS₂ electrode was also prepared as follows: 4 mg commercially bulk-MoS₂ and 20 μ L Nafion solution were dispersed in 1 mL deionized water and sonication for 60 min to form a homogeneous ink, and then 20 μ L dispersion was drop cast onto the GCE and dried at room temperature. As for composite catalyst system, a platinum sheet was used as the counter electrode. The working electrodes were prepared as follows: 10 mg photocatalyst (CdS and 1T-MoS₂-C) were dispersed into a solution containing 100 μ L Nafion, 400 μ L ethanol and 500 μ L water by 60 min sonication to prepare a homogeneous slurry. Then, 40 μ L of the slurry was dropped onto the pretreated indium tin oxide (ITO) conductive glass with an exposed area of 1.0 cm² (1 cm \times 1 cm). A 300 W metal halide lamp equipped with a 420 nm cut-off optical filter was adopted as the light source. The photocurrent density-voltage (I-V) curves were obtained in the bias sweep range -1 to 0 V. The on-off light photoresponse and electrochemical impedance spectroscopy (EIS) were recorded at the open-circuit potential and the frequency range was fixed from 10⁻² to 10⁵ Hz. Mott-Schottky plots were measured under direct current potential polarization at 10³ Hz.

2.4. Photocatalytic H₂ evolution

Photocatalytic H₂ production experiments were carried out in an outer irradiation type photoreactor (50 mL quartz glass) in a N₂ environment. 2 mg 1T-MoS₂-C composite photocatalyst was dispersed in 20 mL aqueous solution containing 10 vol% lactic acid for further photocatalytic H₂ production experiment. Before irradiation, the photocatalytic system was thoroughly degassed to remove air by bubbling N₂ for 30 min. The irradiation light source used in this study was a 500 W metal halide lamp (Perfect Light, Beijing), which is equipped with an optical filter ($\lambda > 420$ nm) to cut off the light in the ultraviolet region. The evolved gas was analyzed by a gas chromatograph (GC-TP2080, BFTP, China, TCD, N₂ as carrier). For comparison, the HER performance of other MoS₂ involved was also performed by attachment of bulk-MoS₂, MoS₂ QDs-200 and MoS₂ QDs-220 on CdS (noted as bulk-MoS₂-C, MoS₂-200-C and MoS₂-220-C), respectively. To obtain the apparent quantum yield (AQY) values of photocatalysts, H₂ production experiments were performed under the designated monochromatic light adjusted by a series of band pass filters (420, 450, 500, 550, 600 and 700 nm). The AQY is estimated using the following equation:

$$\text{AQY (\%)} = (2n_{\text{H}_2}N_A h c) / (t \lambda I A) \cdot 100\%$$

Where n_{H_2} is the hydrogen evolution (mol), N_A is the Avogadro constant (6.02×10^{23}), h is the Planck constant (6.63×10^{-34} J·s), c is the speed of light (3.0×10^8 m·s⁻¹), t is the irradiation time (3600 s), λ is the illumination wavelength (m), I is the illumination intensity (W·m⁻²) determined with a ray virtual radiation actinometer, A is the irradiation area (4.0×10^{-4} m²). Herein, the weight of two photocatalysts (CdS and 3 wt.% 1T-MoS₂-C) is both 4.0×10^{-3} g and the measured values including I , n_{H_2} and AQY are listed in Table S1.

3. Results and discussion

3.1. Structure and property of cocatalysts

MoS₂ QDs hydrothermally synthesized at different reaction temperatures of 180 °C, 200 °C and 220 °C were characterized to investigate the effect of reaction temperature on crystal phase and microstructure of the final products. Raman spectra analysis is the powerful method to determine the phase and number of MoS₂ QDs layers [41,43]. The Raman bands at 146 cm⁻¹, 236 cm⁻¹, and 335 cm⁻¹, previously referred to J₁, J₂, and J₃, correspond to modes that are active in 1T-phase MoS₂ but not allowed in 2H-phase MoS₂ [44,45]. Fig. 2a shows Raman spectra for bulk-MoS₂ and hydrothermal synthesized MoS₂ QDs. Apparently, no Raman peaks in the three shade regions occur in bulk-MoS₂ and MoS₂ QDs-220 samples, indicating that bulk-MoS₂ and MoS₂ QDs-220 both exhibit the 2H-phase trigonal prismatic structure. As the hydrothermal temperature decreases, the intensity of Raman peaks in the three shade regions gradually increases. Particularly, 1T-MoS₂ QDs-180 exhibits dominant Raman bands in the shade regions, with an indication of 1T-phase octahedral prismatic structure. From Fig. 2b, one can see that two obvious peaks of bulk-MoS₂ correspond to the lower energy out-of-plane vibration E_{2g} at 379.2 cm⁻¹ mode and the high energy in-plane vibration A_{1g} at 405.0 cm⁻¹, and the frequency difference in the two characteristic bands is 25.8 cm⁻¹. Note that the A_{1g} mode is clearly negatively shifted from bulk-MoS₂ to MoS₂ QDs-220, MoS₂ QDs-200 and 1T-MoS₂ QDs-180, and accordingly the frequency difference between A_{1g} and E_{2g} modes is clearly narrowed from 25.8 cm⁻¹ for bulk-MoS₂ to 23.9 cm⁻¹ for MoS₂ QDs-220, 24.1 cm⁻¹ for MoS₂ QDs-200, and 22.1 cm⁻¹ for 1T-MoS₂ QDs-180. Such a distinct decrease in frequency difference between E_{2g} and A_{1g} modes indicates the layer number of 1T-MoS₂ QDs-180 is rather thin, with only single- or few-layer thickness [46].

XPS was employed to investigate the chemical compositions of samples. The spectra of Mo 3d of 1T-MoS₂ QDs-180, MoS₂ QDs-200 and

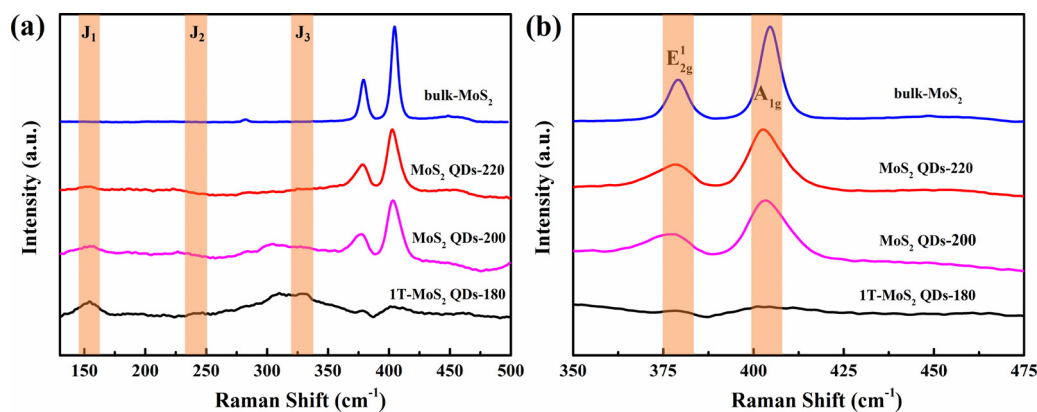


Fig. 2. (a&b) Raman spectra of bulk-MoS₂, MoS₂ QDs-220, MoS₂ QDs-200 and 1T-MoS₂ QDs-180.

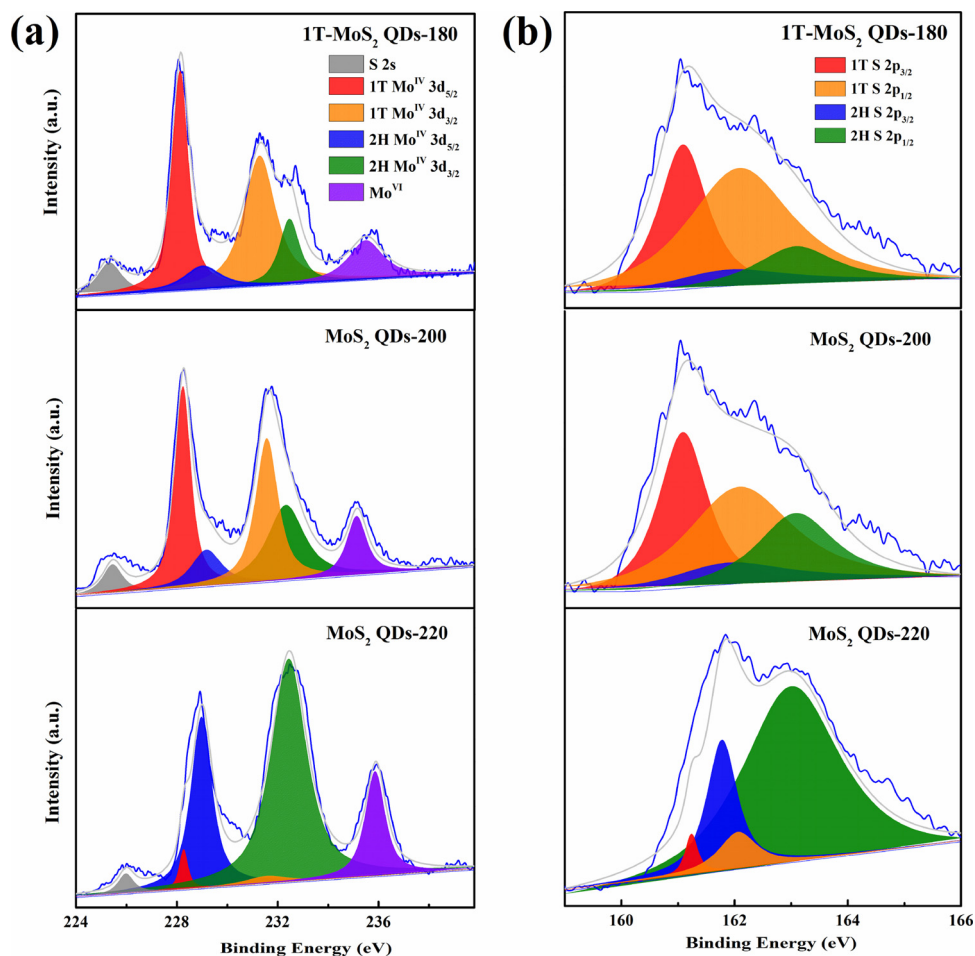


Fig. 3. High-resolution XPS spectra of (a) Mo 3d and (b) S 2p for 1T-MoS₂ QDs-180, MoS₂ QDs-200 and MoS₂ QDs-220.

MoS₂ QDs-220 are shown in Fig. 3a. The peaks located at 229.1 eV (Mo 3d_{5/2}) and 232.3 eV (Mo 3d_{3/2}) indicate +4 oxidation state of 2H-phase MoS₂, and the peaks at 228.2 and 231.4 eV suggest the formation of 1T-phase MoS₂ [47,48]. Fig. 3b shows the spectra of S 2p of samples, in which the peaks at 161.2 eV (S 2p_{3/2}) and 162.1 eV (S 2p_{1/2}) represent the 1T-phase MoS₂, and the peaks at 161.9 eV (S 2p_{3/2}) and 163.0 eV (S 2p_{1/2}) represent the 2H-phase MoS₂. Obviously, MoS₂ QDs prepared at different temperatures are composed of both 1T and 2H phases. To determine the concentrations of 1T-phases in all three samples, the XPS spectra were analyzed by multi-peak curve fitting [48]. Impressively, the highest 1T content was found to be in 1T-MoS₂ QDs-180, which is as high as ~82.4%. With the increase of preparation temperature, the

content of 1T-phase decreases to ~68.1% for MoS₂ QDs-200 and ~6.6% for MoS₂ QDs-220. The results show that reaction temperature decrease would lead to conversion of 2H-phase to 1T-phase during hydrothermal synthesis of MoS₂ QDs, which is in good agreement with the previous report about MoS₂ nanosheets [49]. Furthermore, valence-band (VB) position of 1T-MoS₂ QDs-180 is estimated by VB-XPS spectrum to be 0 eV (Fig. S2a), indicating that 1T-MoS₂ QDs-180 belongs to metallic phase [50,51]. Moreover, the UV-vis spectrum gives a smooth line without any obvious absorption band (Fig. S2b), further confirming the metallic characteristics of 1T-MoS₂ QDs-180. The 1T-MoS₂ QDs-180 aqueous solution shows a brown color (inset in Fig. S2b), analogous to the reported metallic MoS₂ nanosheets [52].

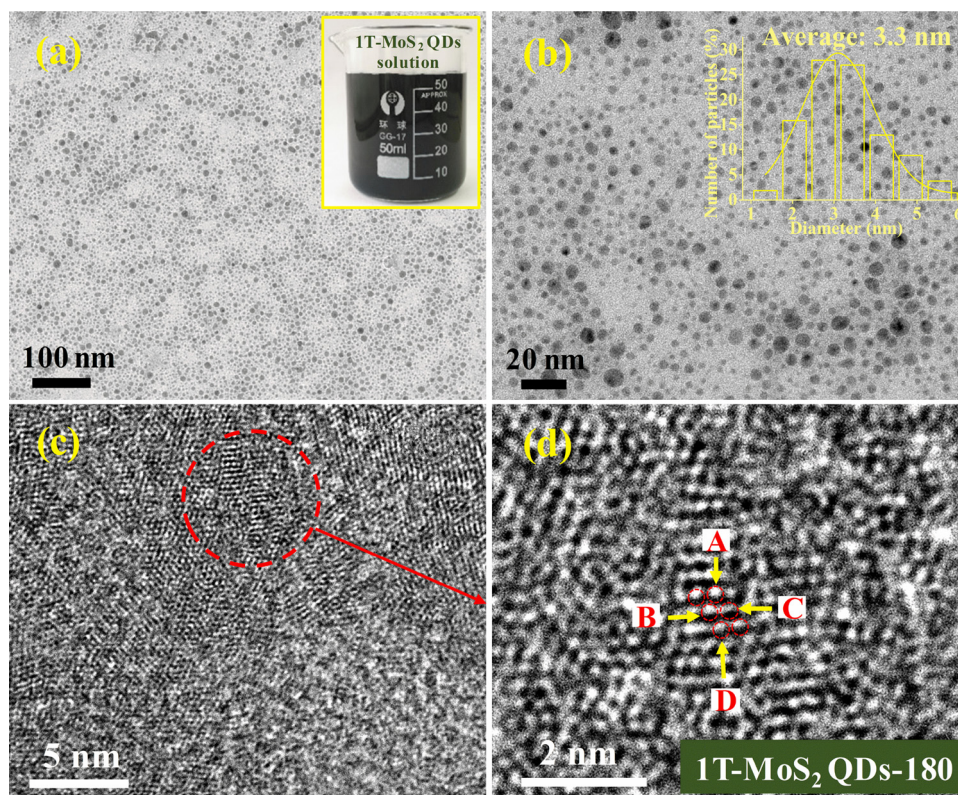


Fig. 4. (a&b) TEM images of 1T-MoS₂ QDs-180. Inset in (a): The photograph of 1T-MoS₂ QDs-180 solution. Inset in (b): The size distribution of 1T-MoS₂ QDs-180. (c) HRTEM image of 1T-MoS₂ QDs-180. (d) Image of the region enclosed by the circle of (c).

TEM was used to characterize the size and microstructure of 1T-MoS₂ QDs-180 (Fig. 4). Obviously, 1T-MoS₂ QDs-180 is distributed uniformly without obvious aggregation (Fig. 4a). The Zeta potential of the 1T-MoS₂ QDs-180 aqueous solution is measured as -21.1 mV (Fig. S3). The presence of abundant negative surface charge on 1T-MoS₂ QDs-180 is beneficial to the good dispersion of 1T-MoS₂ QDs-180 in water and thus forms a homogenous solution in the absence of surfactants (inset in Fig. 4a) [40]. Fig. 4b shows that 1T-MoS₂ QDs-180 possess well-dispersed ultrasmall average size of ~3.3 nm. From the HRTEM image (Fig. 4c), no common (002) lattice plane of crystalline MoS₂ occurs, indicating that 1T-MoS₂ QDs-180 contains single-layer or very a few layers [38]. Further, Mo atoms on the basal plane have a Mo-Mo distance from A to B of 0.27 nm, A to C of 0.34 nm and A to D of 0.56 nm (Fig. 4d), proving the metallic 1T-phase of 1T-MoS₂ QDs-180 [52,53]. From the AFM height profile (Fig. S4), one can observe that 1T-MoS₂ QDs-180 possesses a uniform thickness of 1~1.7 nm, also suggesting its monolayer or very a few layers [54,55]. Besides, BET specific surface area of 1T-MoS₂ QDs-180 powder was measured to ~136.76 m²/g (Fig. S5), which is far higher than that of bulk-MoS₂ (9.14 m²/g). Such a high specific surface area of 1T-MoS₂ QDs-180 would be beneficial for H₂ production because of its abundant active edge sites to the reactants.

Considering the existence of the high-percentage metallic 1T-phase, excellent electrochemical performances are strongly expected over 1T-MoS₂ QDs-180 [56]. Fig. 5a compares the electrocatalytic activity among bulk-MoS₂ and MoS₂ QDs prepared at different temperatures. It is obvious that the as-prepared 1T-MoS₂ QDs-180 shows an excellent HER activity with a lowest onset overpotential and a largest cathodic current density, demonstrating the best catalytic activity of 1T-MoS₂ QDs-180 among all samples. Moreover, 1T-MoS₂ QDs-180 also shows an excellent long-term stability (Fig. S6). Besides, EIS was also conducted to provide further insight into the electrode kinetics during catalytic process. As shown in Fig. 5b, the Nyquist plots show a

dramatically decreased charge-transfer resistance (R_{ct}) for the 1T-MoS₂ QDs-180 relative to bulk-MoS₂, MoS₂ QDs-200 and MoS₂ QDs-220, resulting in fastest electron transfer between 1T-MoS₂ QDs-180 and the electrode for the HER. Obviously, 1T-MoS₂ QDs-180 exhibits excellent electrochemical performances, which may beneficial to the photocatalytic HER [57].

3.2. Morphology, structure and optical property of hybrid catalysts

The heterostructure photocatalysts i.e. 1T-MoS₂-C was obtained via a surface charge promoted self-assembly method driven by strong electrostatic attraction between the positively charged CdS and negatively charged 1T-MoS₂ QDs-180 (Fig. S3). The crystalline structure of 1T-MoS₂-C nanohybrids with varying loadings of 1T-MoS₂ QDs-180 (0, 0.5, 1, 3, 5, 7 wt.%) was further investigated by XRD. As shown in Fig. 6, the diffraction peaks of pure CdS and 1T-MoS₂-C heterostructures at 24.8°, 26.5°, 28.2°, 36.6°, 43.7°, 47.9° and 51.9° can be well-indexed to (100), (002), (101), (102), (110), (103) and (112) planes of hexagonal CdS (JCPDS card No. 02-0549). No additional diffraction peaks can be clearly identified for 1T-MoS₂ QDs-180, even for 7 wt.% 1T-MoS₂-C, suggesting that 1T-MoS₂ QDs-180 in final products is low loading and/or low crystalline [58,59]. UV-vis diffuse reflectance spectra measurement were performed to study the optical property of samples (Fig. 7). It is obvious that loading the 1T-MoS₂ QDs-180 cocatalysts onto the surface of CdS can increase the absorption of catalysts in visible light region from 520 to 800 nm and the absorption of 1T-MoS₂-C composites is enhanced with the increase of 1T-MoS₂ QDs-180 content. This is in accordance with the color change of samples from light yellow to greenish (insert pictures in Fig. 7). The enhanced light absorption of 1T-MoS₂-C composites is favorable to produce more photo-generated electrons and holes, which means that more photo-generated electrons can participate in the reaction and thus enhance the photocatalytic activity [60].

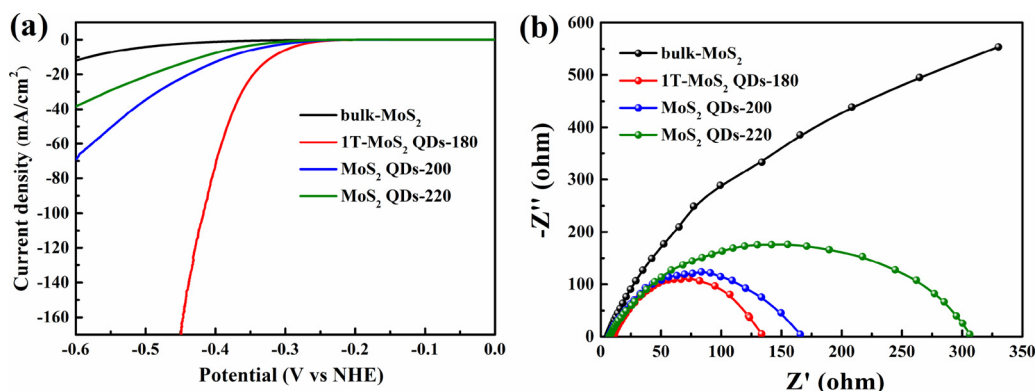


Fig. 5. Electrochemical properties. (a) I-V curves and (b) EIS Nyquist plots of bulk-MoS₂, 1T-MoS₂ QDs-180, MoS₂ QDs-200, MoS₂ QDs-220.

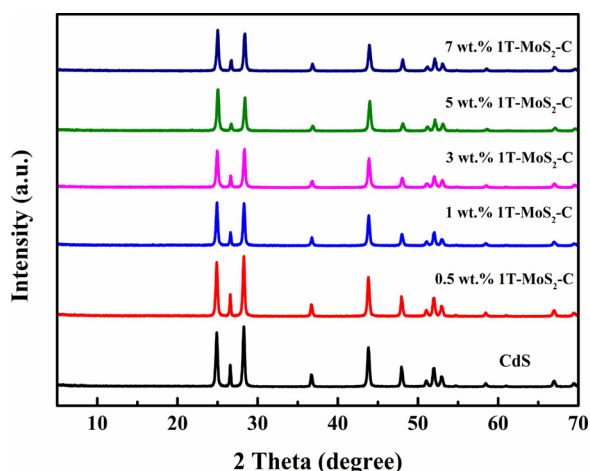


Fig. 6. XRD patterns of CdS and 1T-MoS₂-C photocatalysts containing different amounts of 1T-MoS₂ QDs-180 (0.5, 1, 3, 5, 7 wt.%).

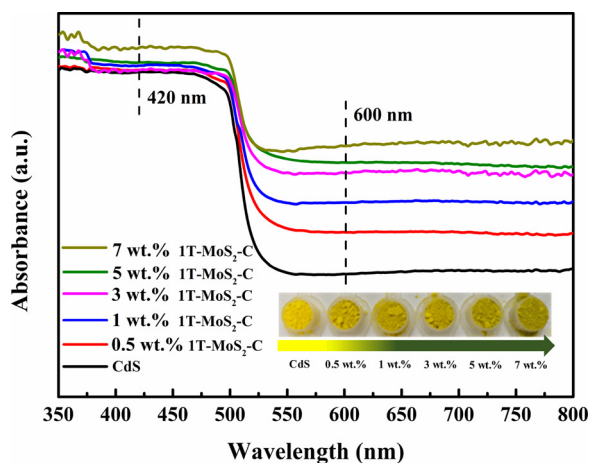


Fig. 7. UV-vis light absorption spectra of CdS and 1T-MoS₂-C heterostructure photocatalysts containing different amounts of 1T-MoS₂ QDs-180 (0.5, 1, 3, 5, 7 wt.%). Inset: color change of samples.

In order to further visualize the morphology and microstructure of the as-prepared 1T-MoS₂-C heterostructures, TEM and HRTEM images have been employed to investigate pure CdS and the 3 wt.% 1T-MoS₂-C sample as an example. As displayed in Fig. S7, pure CdS exhibits 1D rod-shaped morphology, with an interlayer spacing of 0.36 nm that corresponds to the (100) plane of hexagonal CdS [7]. As for the 3 wt.% 1T-MoS₂-C sample, the TEM image in Fig. 8a shows the nanorod morphology similar to pure CdS. However, the magnified HRTEM image

discovers that plenty of dot-like structures in a diameter of several nanometers decorating on nanorods (Fig. 8b). Moreover, close TEM observation indicates that these nanodots are closely attached on the surface of nanorod (Fig. 8c–f), which should be favorable to the electron transfer between two components and thus boost the photocatalytic activity. Besides, HRTEM image in Fig. 8g presents the continuous long-range lattice fringes with a distance of 0.36 nm on the nanorod part, corresponding to the d-spacing of (100) planes of hexagonal CdS. Most importantly, the atomic arrangement of Mo in 1T-MoS₂ QDs-180 is also consistent with the aforementioned one (Fig. 4d), revealed that 1T-MoS₂ QDs-180 still keeps its metallic 1T-phase after combining with CdS [52]. The EDS mappings (Fig. S8) analysis of 3 wt.% 1T-MoS₂-C sample displays the uniform distribution of Cd, Mo and S, further confirming that 1T-MoS₂ QDs-180 is successfully loaded on the surface of CdS. The corresponding atomic mass ratio of Mo:S:Cd is 1:6.69:46.22 (Fig. S9), namely, the mass ratio of MoS₂ and CdS is about 2.8:100, which is consistent with our initial amount added.

3.3. Photocatalytic HER activities

The photocatalytic H₂ production rates of samples was measured under visible light irradiation ($\lambda > 420$ nm) with lactic acid as sacrificial reagent (Figs. 9 and S10). Figs. 9a and S10 show the comparison of photocatalytic H₂ production activities of 1T-MoS₂ QDs-180, CdS, and 1T-MoS₂-C with different amounts of cocatalyst (0.5, 1, 2, 3, 4, 5, 7 wt.%). It can be seen that almost no H₂ is detected when 1T-MoS₂ QDs-180 alone is used as a photocatalyst, suggesting its poor photocatalytic HER activity. The pure CdS sample exhibits an extremely low photocatalytic H₂ production rate of 2.0 mmol h⁻¹ g⁻¹, arising from its poor charge separation and transfer capability. Upon introducing 1T-MoS₂ QDs-180 into CdS to form heterostructures, the photocatalytic HER activity is significantly boosted, and the H₂ evolution rate enhances to a maximum value with increasing 1T-MoS₂ QDs-180 loading up to an optimum level of 3 wt.%. Further increasing the content of 1T-MoS₂ QDs-180 in the heterostructures leads to a decrease of H₂ evolution activity probably due to the masking effect of MoS₂ [61,62]. Under optimized conditions, as shown in Fig. 9b, 3 wt.% 1T-MoS₂-C shows the highest photocatalytic HER rate (131.7 mmol h⁻¹ g⁻¹), much far higher than that of 3 wt.% bulk-MoS₂-C (32.0 mmol h⁻¹ g⁻¹). Such an extraordinary activity of 3 wt.% 1T-MoS₂-C also far exceeds that of conventional Pt/CdS (67.0 mmol h⁻¹ g⁻¹), 3 wt.% MoS₂-200-C (116.0 mmol h⁻¹ g⁻¹) and 3 wt.% MoS₂-220-C (75.0 mmol h⁻¹ g⁻¹). To the best of our knowledge, our home-made 1T-MoS₂-C photocatalyst shows the advanced visible-light-driven HER performance among reported MoS₂/CdS photocatalytic systems (Fig. S11). Besides, the stability assays (Fig. 9c) show that after four runs 3 wt.% 1T-MoS₂-C still exhibits good catalytic stability. Moreover, photocatalytic H₂ production catalyzed by 3 wt.% 1T-MoS₂-C are measured under a prolonged visible light irradiation ($\lambda > 420$ nm) for 25 h (Fig. 9d), and no obvious decay

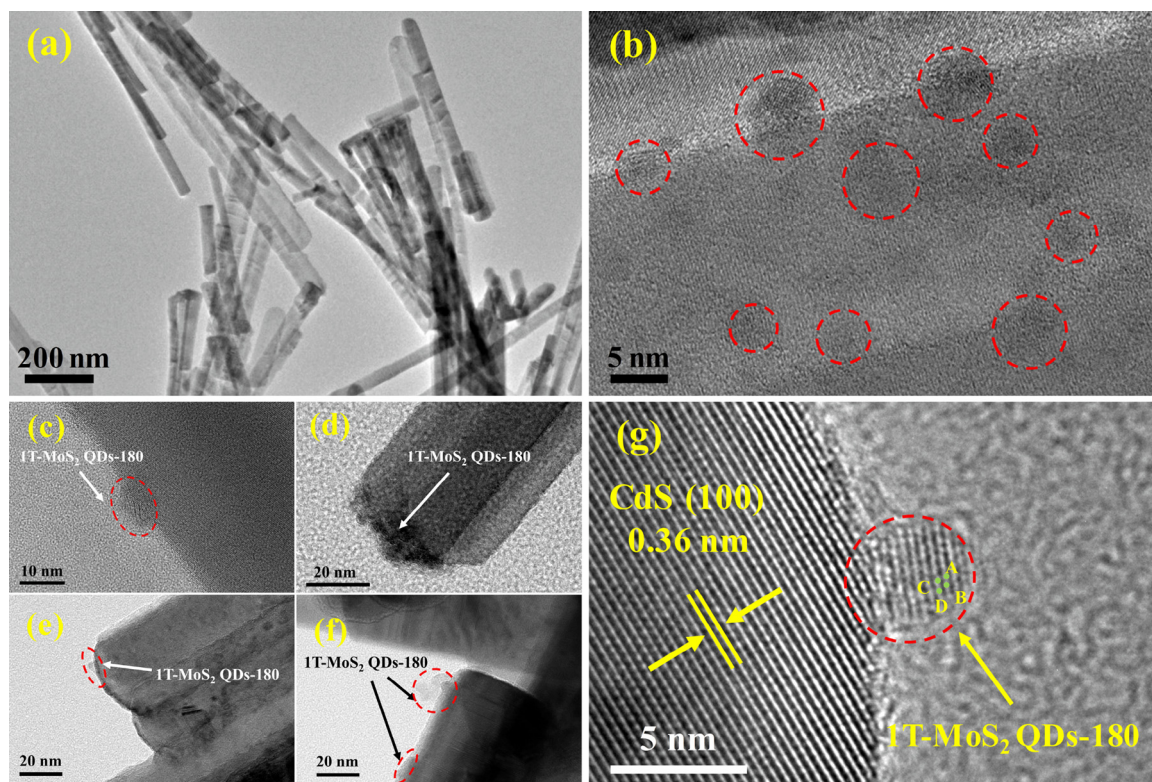


Fig. 8. (a) TEM image and (b–g) HRTEM images of 3 wt.% 1T-MoS₂-C.

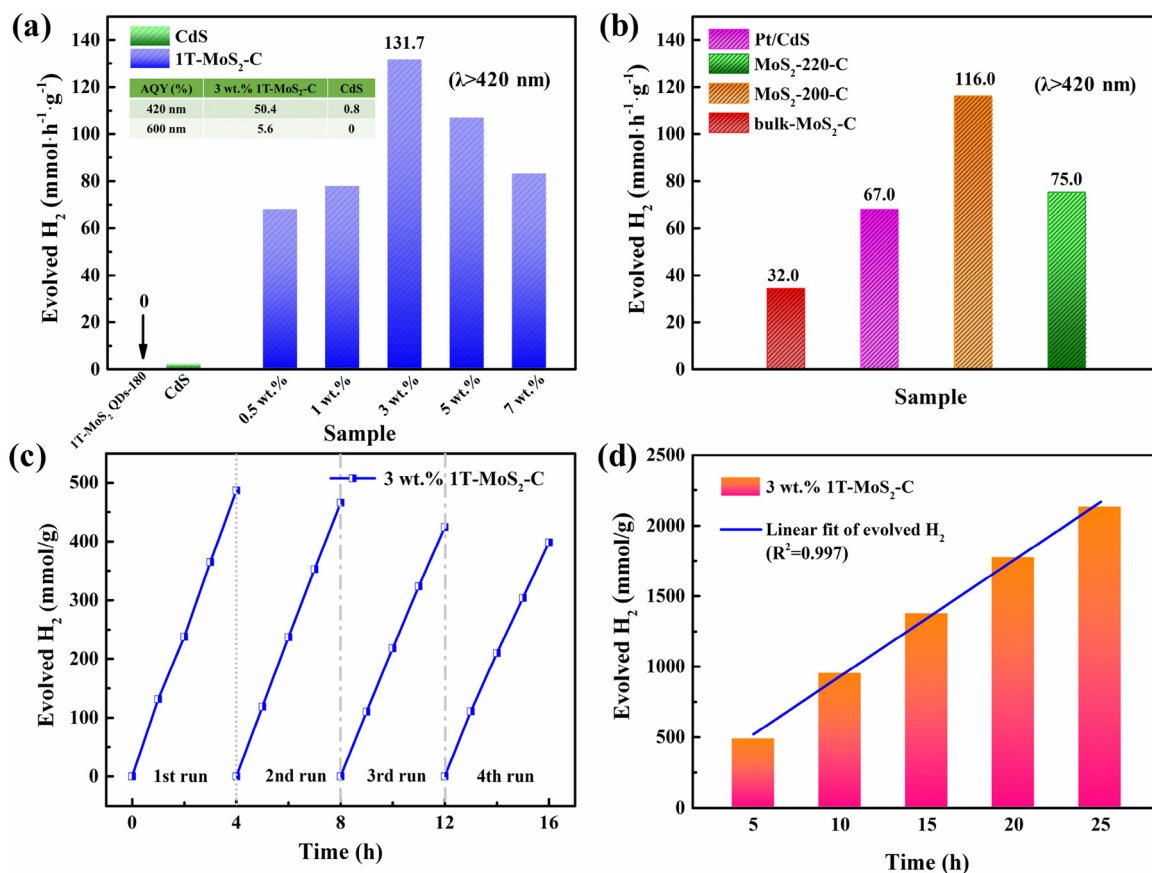


Fig. 9. (a) Photocatalytic H₂ evolution rate of 1T-MoS₂ QDs-180, CdS and 1T-MoS₂-C containing different amounts of cocatalyst (0.5, 1, 3, 5, 7 wt.%) under visible light irradiation. Inset table shows wavelength-dependent AQY of 3 wt.% 1T-MoS₂-C and pure CdS. (b) Photocatalytic H₂ evolution rate of 3 wt.% bulk-MoS₂-C, 3 wt.% Pt/CdS, 3 wt.% MoS₂-220-C and 3 wt.% MoS₂-200-C. (c) Cyclic H₂ production of 3 wt.% 1T-MoS₂-C (λ > 420 nm). (d) Photocatalytic H₂ production catalyzed by 3 wt.% 1T-MoS₂-C under a prolonged visible light (λ > 420 nm) irradiation of 25 h.

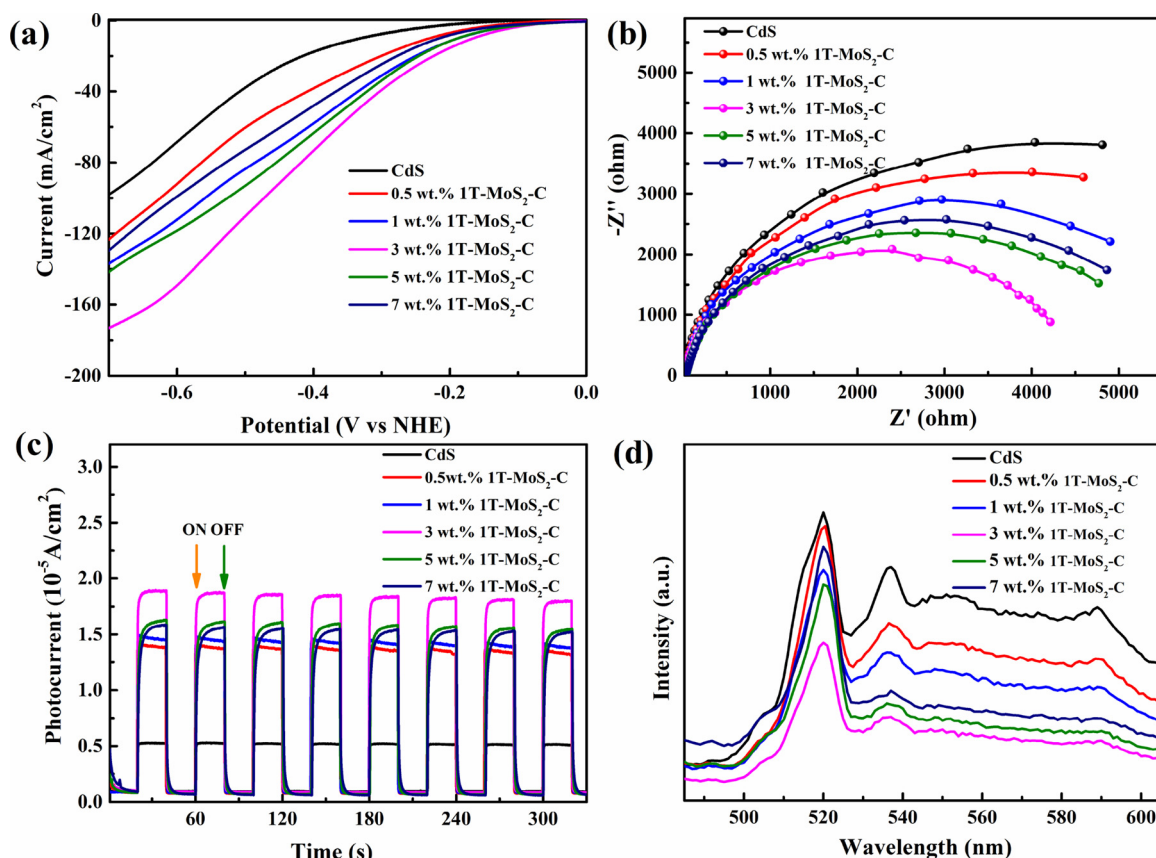


Fig. 10. (a) I-V curves, (b) EIS Nyquist plots, (c) Transient photocurrent responses, and (d) PL spectra of CdS and 1T-MoS₂-C photocatalysts containing different amounts of 1T-MoS₂ QDs-180 (0.5, 1, 3, 5, 7 wt.%).

of photocatalytic HER is discerned, suggesting good durability and practical application for 3 wt.% 1T-MoS₂-C. Furthermore, the AQY of the photocatalytic H₂ evolution of CdS and 3 wt.% 1T-MoS₂-C was measured under various monochromatic light irradiation conditions (Fig. S12 and Table S1). As can be seen in the inset table of Fig. 9a, the AQY of 3 wt.% 1T-MoS₂-C (50.4% at 420 nm and 5.6% at 600 nm), which are both higher than that of CdS (0.8% at 420 nm and 0% at 600 nm). Note that the AQY values of 1T-MoS₂-C at 550 and 600 nm in Fig. S12b are higher than the corresponding absorption, which is due to the up-conversion property of as-prepared 1T-MoS₂ QDs-180 (see PL spectra in Fig. S13).

3.4. Origin and discussion of the enhanced performance

To explore reasons for this significant enhancement of the photocatalytic HER over 1T-MoS₂-C heterostructure, we then performed a series of careful characterizations for pure CdS and 1T-MoS₂-C samples. The photoelectrochemical performance assays including I-V, EIS and transient photocurrent responses may offer efficient evidence for confirming the electron-hole pair separation and transfer in the composite photocatalysts. The polarization curves (Fig. 10a) shows an increased current density in all 1T-MoS₂-C samples as compared with pure CdS, indicating that 1T-MoS₂ QDs-180 can efficiently promote the reduction of water to H₂ on 1T-MoS₂-C [60]. The loading-dependent photoresponses show that 3 wt.% 1T-MoS₂-C has a highest current density, which is consistent with the results of photocatalytic HER performance (Fig. 9a). Fig. 10b shows that 3 wt.% 1T-MoS₂-C presents a representative EIS Nyquist plot with a smallest diameter under light illumination, indicating efficient interfacial charge-carrier transfer in this 3 wt.% 1T-MoS₂-C heterostructure [41]. The transient photocurrent responses (Fig. 10c) of CdS and 1T-MoS₂-C photocatalysts with 20 s

under visible light irradiation on/off cycles, show that the photocurrent of 3 wt.% 1T-MoS₂-C is superior to that of pure CdS and other 1T-MoS₂-C photocatalysts, beneficial to the generation and transfer of electrons and holes. Also, the photocurrent responses are stable and highly reproducible for several on-off cycles.

PL emission spectra, a useful technique to monitor the photo-generated charge recombination in form of PL emission, were recorded to explore the charge trapping and separation in 1T-MoS₂-C heterostructures. PL spectra of photocatalysts were measured at 426 nm excitation. Fig. 10d shows the fluorescence spectra of pure CdS and 1T-MoS₂-C with different 1T-MoS₂ QDs-180 loading contents. Two fluorescence peaks appearing at ~520 nm and ~590 nm are assigned to near-band-edge and band-to-band emission of CdS, respectively [63,64]. The peak at ~538 nm is associated with structural defects arisen from the core defects on the CdS nanorods surfaces [63]. Pure CdS shows a strong emission attributable to its high recombination of photoexcited charges. Upon loading 1T-MoS₂ QDs-180, the emissions are remarkably quenched due to fast electron transfer from CdS to 1T-MoS₂ QDs-180, which can efficiently suppress the electron-hole recombination within CdS and hence enhance the photocatalytic activity. The lowest PL intensity can be observed by 3 wt.% 1T-MoS₂-C, which is in good agreement with its optimal H₂ evolution activity (Fig. 9a). The above photoelectrochemical/photochemical analyses assays (I-V, EIS, the transient photocurrent responses, and PL) demonstrate that the photocarrier separation and transfer of 3 wt.% 1T-MoS₂-C is remarkably improved, and as a consequence of enhanced photocatalytic H₂ evolution performance.

To investigate the photocatalytic mechanism of 1T-MoS₂-C, Mott-Schottky plots were measured to estimate the conduction band (CB) levels of 1T-MoS₂ QDs-180 and CdS. As can be found in Fig. 11a&b, the flat-band potentials are estimated to be -0.50 V and -0.30 V vs. SCE for

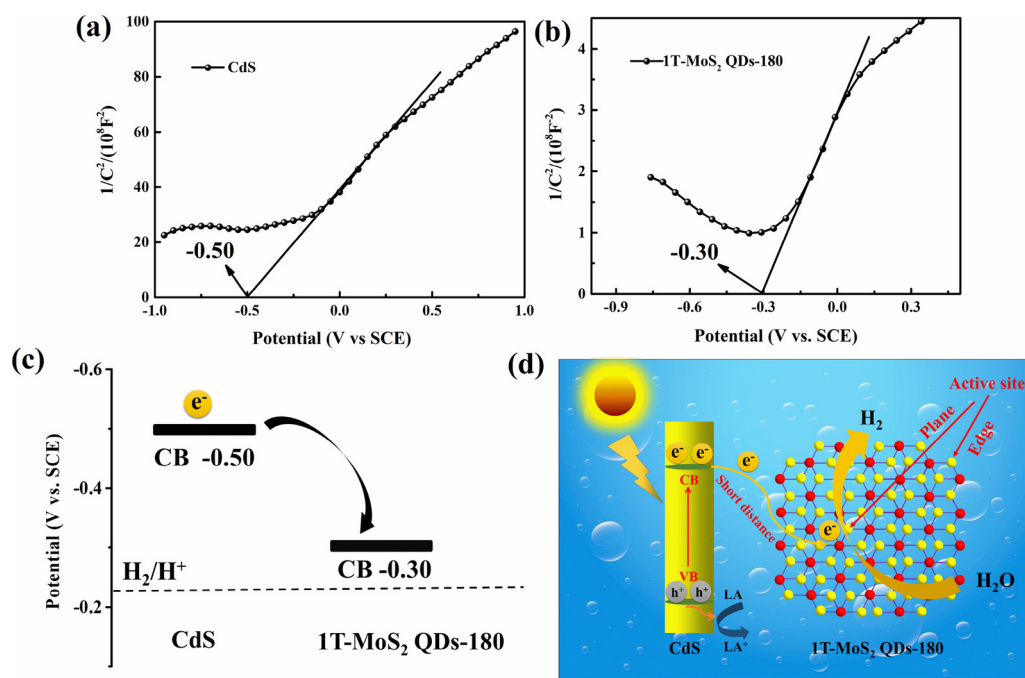


Fig. 11. Photocatalytic HER mechanism. Mott-Schottky plots of (a) CdS and (b) 1T-MoS₂ QDs-180. (c) Schematic illustration of the band structure of CdS and 1T-MoS₂ QDs-180. (d) Schematic illustration of the photogenerated charge transfer in the 1T-MoS₂-C heterostructure under visible light irradiation ($\lambda > 420$ nm).

CdS and 1T-MoS₂ QDs-180, respectively. In general, the flat-band potential can be used to approximately estimate the CB position. Obviously, the CB potential of 1T-MoS₂ QDs-180 has a positive shift of 0.2 eV compared with CdS. According to the H₂ evolution “band matching” theory [65], the photo-excited electrons from CdS would be injected into the CB of 1T-MoS₂ QDs-180 because of lower and favorable energy level of 1T-MoS₂ QDs-180 (Fig. 11c). Based on the above results, the photocatalytic HER process of 1T-MoS₂-C heterostructure under the visible-light irradiation is schematically displayed in Fig. 11d. Typically, under visible light illumination, electron-hole pairs are generated in CdS. With intimate contact between the CdS and 1T-MoS₂ QDs-180, the photo-excited electrons rapidly transfer from the CB of CdS to the lower CB of 1T-MoS₂ QDs-180 cocatalyst. In the 1T-MoS₂-C heterostructure, small-sized 1T-MoS₂ QDs-180 nanodots well attaching on the CdS facilitates electron transfer from CdS to 1T-MoS₂ QDs-180 in a shorted distant. Furthermore, high electrical conducting 1T-MoS₂ QDs-180 can rapidly transfer electron to the surface. The abundant in-plane active sites of 1T-MoS₂ QDs-180 can serve as the electron reservoirs and simultaneously offer reaction sites for H₂ production. All these favorable merits originating from ultrasmall size effect and high percentage 1T-phase of 1T-MoS₂ QDs-180. Meanwhile, the photo-generated holes in the valence band of CdS can be consumed by the sacrificial reagents (lactic acid). Consequently, the photo-generated electrons and holes can be effectively separated, which can largely promote the photocatalytic H₂ evolution activity of 1T-MoS₂-C heterostructure.

4. Conclusions

In summary, a facile one-step hydrothermal method has been adopted for preparation of ultrasmall-sized (with average size of ~ 3.3 nm), high-percentage (over 82%) 1T-phase MoS₂ quantum dots at a temperature of 180 °C. The obtained 1T-MoS₂ QDs-180 subsequently used as effective cocatalysts for visible-light photocatalytic H₂ evolution over CdS nanorods. Benefiting from the abundance of exposed catalytic edge sites and the excellent intrinsic conductivity of 1T-MoS₂ QDs-180, the preformed 1T-MoS₂-C heterostructure photocatalysts exhibit remarkably enhanced visible-light photocatalytic HER in

comparison with pure CdS. Specifically, an optimized 3 wt.% 1T-MoS₂-C achieves a remarkable enhanced visible light ($\lambda > 420$ nm) photocatalytic H₂ production rate of 131.7 mmol h⁻¹ g⁻¹, which is obviously higher than that of commonly-used Pt/CdS (67.0 mmol h⁻¹ g⁻¹), and also far higher than that of pure CdS (2.0 mmol h⁻¹ g⁻¹) as well as bulk-MoS₂-C (32.0 mmol h⁻¹ g⁻¹). Meanwhile, such an H₂ production rate exceeds all reported phase-engineered MoS₂ photocatalytic systems. This increased HER performance can be attributed to the following aspects of reasons: 1) as a cocatalyst, 1T-MoS₂ QDs-180 co-operating with CdS can increase light absorption and lower the activation barriers for H₂ evolution; 2) 1T-MoS₂ QDs-180 owns excellent electrical conductivity and abundant active sites, which is beneficial to H₂ evolution; 3) favorable band position between the 1T-MoS₂ QDs-180 and CdS can effectively enhance transfer ability of charge and thus inhibit the recombination of electron-hole pairs. Most importantly, this work offers an effective protocol to fabricate 1T-MoS₂ QDs cocatalyst with high-density active sites and high conductivity, which is not only appropriate in the photocatalytic HER but also extendable for energy conversion/storage and biological applications.

Acknowledgement

The work was supported by the National Natural Science Foundation of China (Nos. 21476019, 21676017).

Appendix A. Supplementary data

Supplementary material related to this article can be found, in the online version, at doi:<https://doi.org/10.1016/j.apcatb.2018.10.033>.

References

- [1] A. Fujishima, K. Honda, *Nature* 238 (1972) 37.
- [2] M. Ni, M.K. Leung, D.Y. Leung, K. Sumathy, *Renew. Sustain. Energy Rev.* 11 (2007) 401–425.
- [3] X. Chen, S. Shen, L. Guo, S.S. Mao, *Chem. Rev.* 110 (2010) 6503–6570.
- [4] J. Xie, C. Yang, M. Duan, J. Tang, Y. Wang, H. Wang, J. Courtois, *Ceram. Int.* 44 (2018) 5459–5465.
- [5] H.B. Fang, X.H. Zhang, J. Wu, N. Li, Y.Z. Zheng, X. Tao, *Appl. Catal. B: Environ.* 225 (2017) 397–405.

- [6] J. Low, J. Yu, M. Jaroniec, S. Wageh, A.A. Alghamdi, *Adv. Mater.* 29 (2017) 1601694.
- [7] N. Li, J. Wu, Y. Lu, Z. Zhao, H. Zhang, X. Li, Y.-Z. Zheng, X. Tao, *Appl. Catal. B: Environ.* 238 (2018) 27–37.
- [8] E.M. Samsudin, S.B.A. Hamid, J.C. Juan, J.B. Wan, G. Centi, *Appl. Surf. Sci.* 370 (2016) 380–393.
- [9] T. Chen, W. Quan, L. Yu, Y. Hong, C. Song, M. Fan, L. Xiao, W. Gu, W. Shi, *J. Alloys. Compd.* 686 (2016) 628–634.
- [10] S. Ma, Y. Deng, J. Xie, K. He, W. Liu, X. Chen, X. Li, *Appl. Catal. B: Environ.* 227 (2018) 218–228.
- [11] Y. Li, H. Wang, L. Xie, Y. Liang, G. Hong, H. Dai, *J. Am. Chem. Soc.* 133 (2011) 7296–7299.
- [12] D. Voiry, M. Salehi, R. Silva, T. Fujita, M. Chen, T. Asefa, V.B. Shenoy, G. Eda, M. Chhowalla, *Nano Lett.* 13 (2013) 6222–6227.
- [13] J. Xie, H. Zhang, S. Li, R. Wang, X. Sun, M. Zhou, J. Zhou, X.W. Lou, Y. Xie, *Adv. Mater.* 25 (2013) 5807–5813.
- [14] Z. Wu, B. Fang, Z. Wang, C. Wang, Z. Liu, F. Liu, W. Wang, A. Alfantazi, D. Wang, D.P. Wilkinson, *ACS Catal.* 3 (2013) 2101–2107.
- [15] G. Ye, Y. Gong, J. Lin, B. Li, Y. He, S.T. Pantelides, W. Zhou, R. Vajtai, P.M. Ajayan, *Nano Lett.* 16 (2016) 1097–1103.
- [16] L. Wei, Y. Chen, Y. Lin, H. Wu, R. Yuan, Z. Li, *Appl. Catal. B: Environ.* 144 (2014) 521–527.
- [17] S. Bai, L. Wang, X. Chen, J. Du, Y. Xiong, *Nano Res.* 8 (2015) 175–183.
- [18] Z. Zhang, L. Huang, J. Zhang, F. Wang, Y. Xie, X. Shang, Y. Gu, H. Zhao, X. Wang, *Appl. Catal. B: Environ.* 233 (2018) 112–119.
- [19] B. Hinnemann, P.G. Moses, J. Bonde, K.P. Jørgensen, J.H. Nielsen, S. Hørch, A. Ib Chorkendorff, J.K. Nørskov, *J. Am. Chem. Soc.* 127 (2005) 5308–5309.
- [20] T.F. Jaramillo, K.P. Jørgensen, J. Bonde, J.H. Nielsen, S. Hørch, I. Chorkendorff, *Science* 317 (2007) 100–102.
- [21] B. Pourabbas, B. Jamshidi, *Chem. Eng. J.* 138 (2008) 55–62.
- [22] C. Liu, L. Wang, Y. Tang, S. Luo, Y. Liu, S. Zhang, Y. Zeng, Y. Xu, *Appl. Catal. B: Environ.* 164 (2015) 1–9.
- [23] J.M. Wu, W.E. Chang, Y.T. Chang, C.K. Chang, *Adv. Mater.* 28 (2016) 3718–3725.
- [24] B. Chen, E. Liu, F. He, C. Shi, C. He, J. Li, N. Zhao, *Nano Energy* 26 (2016) 541–549.
- [25] Y. Yin, J. Han, Y. Zhang, X. Zhang, P. Xu, Q. Yuan, L. Samad, X. Wang, Y. Wang, Z. Zhang, *J. Am. Chem. Soc.* 138 (2016) 7965–7972.
- [26] X. Dai, K. Du, Z. Li, M. Liu, Y. Ma, S. Hui, Z. Xin, Y. Ying, *ACS Appl. Mater. Interfaces* 7 (2015) 27242–27253.
- [27] J. Shi, R. Tong, X. Zhou, Y. Gong, Z. Zhang, Q. Ji, Y. Zhang, Q. Fang, L. Gu, X. Wang, *Adv. Mater.* 28 (2016) 10664–10672.
- [28] X. Xie, T. Makaryan, M. Zhao, K.L. Van Aken, Y. Gogotsi, G. Wang, *Adv. Energy Mater.* 6 (2016) 1502161.
- [29] D. Hou, W. Zhou, X. Liu, K. Zhou, J. Xie, G. Li, S. Chen, *Electrochim. Acta* 166 (2015) 26–31.
- [30] T.-N. Ye, L.-B. Lv, M. Xu, B. Zhang, K.-X. Wang, J. Su, X.-H. Li, J.-S. Chen, *Nano Energy* 15 (2015) 335–342.
- [31] Q. Xiang, J. Yu, M. Jaroniec, *J. Am. Chem. Soc.* 134 (2012) 6575–6578.
- [32] K. Chang, Z. Mei, T. Wang, Q. Kang, S. Ouyang, J. Ye, *ACS Nano* 8 (2014) 7078–7087.
- [33] Y.J. Yuan, Y. Yang, Z. Li, D. Chen, S. Wu, G. Fang, W. Bai, M. Ding, L.X. Yang, D.P. Cao, *ACS Appl. Energy Mater.* 1 (4) (2018) 1400–1407.
- [34] H. Tian, M. Liu, W. Zheng, *Appl. Catal. B: Environ.* 225 (2018) 468–476.
- [35] W. Gu, Y. Yan, C. Zhang, C. Ding, Y. Xian, *ACS Appl. Mater. Interfaces* 8 (2016) 11272–11279.
- [36] W. Qiao, S. Yan, X. Song, X. Zhang, X. He, W. Zhong, Y. Du, *Appl. Surf. Sci.* 359 (2015) 130–136.
- [37] G.D. Mm, D.D. Shaijumon, *ACS Nano* 8 (2014) 5297–5303.
- [38] X. Ren, L. Pang, Y. Zhang, X. Ren, H. Fan, S. Liu, *J. Mater. Chem. A* 3 (2015) 10693–10697.
- [39] J. Sun, L. Duan, Q. Wu, W. Yao, *Chem. Eng. J.* 332 (2018) 449–455.
- [40] C. Tan, Z. Luo, A. Chaturvedi, Y. Cai, Y. Du, Y. Gong, Y. Huang, Z. Lai, X. Zhang, L. Zheng, *Adv. Mater.* 30 (2018) 1705509.
- [41] X.-H. Zhang, N. Li, J. Wu, Y.-Z. Zheng, X. Tao, *Appl. Catal. B: Environ.* 229 (2018) 227–236.
- [42] Z. Sun, H. Zheng, J. Li, P. Du, *Energy Environ. Sci.* 8 (2015) 2668–2676.
- [43] B. Li, L. Jiang, X. Li, P. Ran, P. Zuo, A. Wang, L. Qu, Y. Zhao, Z. Cheng, Y. Lu, *Sci. Rep.* 7 (2017) 11182.
- [44] Z. Lei, J. Zhan, L. Tang, Y. Zhang, Y. Wang, *Adv. Energy Mater.* (2018) 1703482.
- [45] G. Eda, H. Yamaguchi, D. Voiry, T. Fujita, M. Chen, M. Chhowalla, *Nano Lett.* 11 (2011) 5111–5116.
- [46] C. Lee, H. Yan, L.E. Brus, T.F. Heinz, J. Hone, S. Ryu, *ACS Nano* 4 (2010) 2695–2700.
- [47] M.A. Lukowski, A.S. Daniel, F. Meng, A. Forticaux, L. Li, S. Jin, *J. Am. Chem. Soc.* 135 (2013) 10274–10277.
- [48] J.M. Ting, T.X. Nguyen, *Chem. Eur. J.* 23 (2017) 17348–17355.
- [49] X. Geng, Y. Zhang, H. Yang, J. Li, L. Yang, M. Benamara, L. Chen, H. Zhu, *Nano Lett.* 17 (2017) 1825–1832.
- [50] Q. Yue, Y. Wan, Z. Sun, X. Wu, Y.P. Yuan, P. Du, *J. Mater. Chem. A* 3 (2015) 16941–16947.
- [51] K. Chang, X. Hai, H. Pang, H. Zhang, L. Shi, G. Liu, H. Liu, G. Zhao, M. Li, J. Ye, *Adv. Mater.* 28 (2016) 10033–10041.
- [52] X. Geng, W. Sun, W. Wu, B. Chen, A. Al-Hilo, M. Benamara, H. Zhu, F. Watanabe, J. Cui, T.P. Chen, *Nat. Commun.* 7 (2016) 10672.
- [53] Q. Liu, Q. Fang, W. Chu, Y. Wan, X. Li, W. Xu, M. Habib, S. Tao, Y. Zhou, D. Liu, *Chem. Mater.* 29 (2017) 4738–4744.
- [54] H. Li, Q. Zhang, C.C.R. Yap, B.K. Tay, T.H.T. Edwin, A. Olivier, D. Baillargeat, *Adv. Funct. Mater.* 22 (2012) 1385–1390.
- [55] Y. Deng, Z. Luo, N.J. Conrad, H. Liu, Y. Gong, S. Najmaei, P.M. Ajayan, J. Lou, X. Xu, P.D. Ye, *ACS Nano* 8 (2014) 8292–8299.
- [56] L. Cai, W. Cheng, T. Yao, Y. Huang, F. Tang, Q. Liu, W. Liu, Z. Sun, F. Hu, Y. Jiang, *J. Phys. Chem. C* 121 (2017) 15071–15077.
- [57] U. Maitra, U. Gupta, M. De, R. Datta, A. Govindaraj, C.N. Rao, *Angew. Chem.* 125 (2013) 13295–13299.
- [58] X.L. Yin, L.L. Li, W.J. Jiang, Z. Yun, Z. Xiang, L.J. Wan, J.S. Hu, *ACS Appl. Mater. Interfaces* 8 (2016) 15258–15266.
- [59] M.Q. Yang, C. Han, Y.J. Xu, *J. Phys. Chem. C* 119 (2015) 27234–27246.
- [60] B. Han, S. Liu, N. Zhang, Y.J. Xu, Z.R. Tang, *Appl. Catal. B: Environ.* 202 (2017) 298–304.
- [61] L. Shen, M. Luo, Y. Liu, R. Liang, F. Jing, L. Wu, *Appl. Catal. B: Environ.* 166–167 (2015) 445–453.
- [62] Y.J. Yuan, F. Wang, B. Hu, H.W. Lu, Z.T. Yu, Z.G. Zou, *Dalton Trans.* 44 (2015) 10997–11003.
- [63] S. Liu, N. Zhang, Z.R. Tang, Y.J. Xu, *ACS Appl. Mater. Interfaces* 4 (2012) 6378–6385.
- [64] B. Chai, M. Xu, J. Yan, Z. Ren, *Appl. Surf. Sci.* 430 (2017) 523–530.
- [65] B. Qiu, Q. Zhu, M. Xing, J. Zhang, *Chem. Commun.* 53 (2016) 897–900.